DOI: 10.1002/ ((please add manuscript number))
Article type: Full Paper

Laser-assisted Ultrafast Exfoliation of Black Phosphorus in Liquid with Tunable Thickness for Li-ion Batteries

Weiran Zheng[†] Jeongyeon Lee,[†] Zhi-Wen Gao, Yong Li, Shenghuang Lin, Shu Ping Lau, Lawrence Yoon Suk Lee**

Dr. Weiran Zheng; Dr. Jeongyeon Lee; Zhi-Wen Gao; Yong Li; Dr. Lawrence Yoon Suk Lee
Department of Applied Biology and Chemical Technology and the State Key Laboratory of Chemical Biology and Drug Discovery, The Hong Kong Polytechnic University, Hung Hom, Kowloon, Hong Kong, China

Dr. Shenghuang Lin; Dr. Shu Ping Lau
Department of Applied Physics, The Hong Kong Polytechnic University, Hung Hom, Kowloon, Hong Kong, China

E-mail: *apsplau@polyu.edu.hk; lawrence.ys.lee@polyu.edu.hk*

Keywords: *black phosphorus; laser-assisted exfoliation; morphology control; Li-ion battery; morphological effect*

Few-layer black phosphorus (BP) is an emerging two-dimensional (2D) material suitable for energy applications. However, its controllable preparation remains challenging. Herein, we present a highly-efficient route for the scalable production of few-layer BP nanosheets using a pulsed laser in low-boiling point solvents. Changing the laser irradiation time, energy, and solvent type leads to precise control over the layer number and lateral size of the nanosheets with a narrow distribution. The process is understood by a plasma quenching mechanism and interlayer interaction weakened by the *in situ* generated vapor bubbles. The excellent control of the BP nanosheets enables us to study the morphological effect on Li-ion battery performance as anode material: low layer number benefits both charge transfer and Li^+ ion diffusion, while a high aspect ratio can improve the charge transfer but also increase the Li^+ ion diffusion path.

This study delivers insights on the tailored fabrication of thin 2D materials using laser for morphology-dependent electrochemical energy conversion and storage.

1. Introduction

Black phosphorus (BP) is the most thermodynamically stable allotrope of phosphorus, featuring a lamellar structure similar to graphite.[1] As a member of the flourishing two-dimensional (2D) materials family, breaking the weak interlayer van der Waals interaction can exfoliate bulk BP to its few-layer forms. By doing so, desirable physical properties can be achieved, such as tunable bandgap from 0.3 eV (bulk) to 2 eV (monolayer), high surface area, and excellent hole mobility (>800 cm^2 V^{-1} s^{-1}).[2-4] These attractive traits of BP have unleashed its great potential in optoelectronic, semiconductor-based devices, photo(electro)catalysis, and energy storage.[5-8] Especially, as the anode material for Li-ion batteries (LIBs), BP possesses a theoretical capacity of 2596 mAh g^{-1}, which is seven times higher than that of commercially used graphite (372 mAh g^{-1}).[9-11] Therefore, exfoliated few-layer BP with an enlarged surface area makes a promising candidate for high-performance LIBs.

However, the main challenge lies in obtaining thickness-controlled few-layer BP massively and rapidly. Compared with the 'bottom-up' growth of few-layer BP under extreme conditions,[12] 'top-down' strategies, mainly liquid-phase exfoliation (LPE) method,[13] are much more affordable and suitable for scale-up production of few-layer BP. A typical LPE process relies on vigorous agitation (such as thermal treatment, shear, and ultrasonication) of bulk BP in solution to weaken the interlayer interaction and enlarge the interlayer distance.

Currently, ultrasonication is the most popular and convenient approach but suffers a few drawbacks. Firstly, it is usually time-consuming and inefficient, typically requiring 10-24 h to achieve low exfoliation yield up to ~20%.[14] Secondly, due to its structural instability in ambient O_2 and water,[15] few-layer BP is mainly prepared using high-boiling-point and toxic organic solvents, including dimethylformamide, dimethyl sulfoxide, and ionic liquids,[16-18] to

avoid exposure to O_2. Other ingredients, such as sodium dodecyl sulfate (SDS), [19] are often introduced to increase stability and efficiency, exacerbating the post-processes (separation and purification). Thirdly and most problematically, LPE often shows little control over the morphology (lateral size and thickness) of products. Further treatments, such as gradient centrifugation, are commonly involved after LPE to narrow the size and thickness distribution, which further complicates the post-treatment, lowers the efficiency, and increases the risk of compromising the structural integrity.

Such difficulties motivate us to search for other strategies to exfoliate BP in a faster, controllable, and scalable fashion without involving high-boiling point solvents and additives. Laser ablation/irradiation, which has shown the ability of exfoliating graphite to high-quality graphene within several nanoseconds,[20-22] makes a great option. During the irradiation, thermal expansion of interlayer lattice occurs, leading to the production of thinner layers.[23-24] Moreover, laser ablation in liquid (LAL) requires no additive nor specific solvent, enabling the production of surfactant-free products in green solvents. Currently, despite recent attempts of exfoliating BP using a laser,[25] the rapid and morphology-controlled production of exfoliated BP at a massive scale is not yet available.

Herein, we demonstrate the mass production of few-layer BP nanosheets by irradiating pristine BP crystal with a pulsed laser for a few microseconds in a series of low-boiling point solvents including, methanol, ethanol, propanol, and hexane. Without additional ingredients, BP nanosheets with narrow and solvent-dependent thickness distribution and large lateral size are prepared, as well as mono-dispersed nanoparticles identified as amorphous BP. The exfoliation yield reaches 93.7%, the highest value reported to date. The effects of the solvent type, laser irradiation time, and energy on the morphology of produced nanosheets and nanoparticles are studied to understand the mechanism of laser-assisted liquid-phase exfoliation of BP. The thickness-controlled few-layer BP nanosheets are further engaged as an anode in LIB to

investigate its morphological influence on BP-based LIB performance, where the relationship between layer number, lateral size, cycling stability, Li^+ ion transfer kinetics, and diffusivity are discussed. Finally, the half/full-cell performance of BP/graphene-based anode were studied.

2. Results and discussion

2.1. Laser-assisted exfoliation of BP

The experimental setup for liquid-phase laser-assisted exfoliation is depicted in **Figure S1**, Supporting Information (SI). Bulk BP crystal was irradiated in deoxygenated 2-propanol by an Nd:YAG Q-switched pulsed laser (λ = 1,064 nm, 650 mJ) with 8 ns pulse duration and a repetition rate of 10 Hz (total laser duration of 80 ns per second). After irradiation, the solution changed from colorless to dark yellow suspension (**Figure 1A** and Supplementary movie 1 (2.4 μs)), containing laser-treated BP (L-BP) as the product. After repeating the irradiation process, the bulk BP could be fully converted to L-BP, demonstrating the high efficiency and suitability of using the laser-assisted method for scale-up production. Despite using no stabilizing agent, no visible aggregation or restacking was evident after two days under room temperature storage. The morphology of the products was examined by transmission electron microscopy (TEM) and atomic force microscopy (AFM). A typical TEM image of L-BP (**Figure 1D**) features stacked nanosheets and the steps in the edge region (yellow circle). The high-resolution image of the highlighted area (black dotted rectangle) reveals both BP nanosheets and particles. The interplanar spacing (*d* spacing) of 0.252 nm of the nanosheet matches the (111) plane of BP,[26] and the selected area electron diffraction (SAED) pattern of the highlighted region presented in **Figure 1E** agrees with that of exfoliated BP nanosheets,[27] confirming the unaffected BP nanosheet structure. The inner- and inter-layer structural integrity of BP nanosheets are also acknowledged by the high-resolution TEM (HRTEM) images (**Figures 1F** and **1G**), where the crystallographic projections of phosphorus atoms along the (110) and (201) zone axis are

presented. Meanwhile, a minor amorphous region at the edge (yellow arrow and lines) is suggested, similar to a few-layer BP prepared by LPE.[15]

Although TEM shows visual confirmation of the layer structure, AFM can provide precise information on the height and size. By drop-casting the diluted L-BP suspension on a silicon thermal oxide (SiO_2/Si) wafer substrate within a 2-propanol-saturated enclosure (**Figure S2**, SI) to slowly evaporate, a ring stain was formed. AFM analyses reveal thicker flakes (> 20 nm) on the ring edge (**Figure 1H**) and monolayer films (< 7 nm) assembled on the SiO_2 surface inside the ring (**Figure 1I**) as well as smaller nanoparticles. The observation of the nanosheet structure confirms the successful exfoliation of bulk BP crystal to a few-layer BP. The flakes show lateral sizes larger than 5 μm, which is significantly larger than most of the few-layer BP obtained *via* LPE. Furthermore, the BP nanosheets assemble on the wafer in an edge-to-edge manner, other than overlapping or stacking. Such behavior, commonly observed for nanoparticles,[28-29] could be due to the interaction between few-layer BP nanosheets at the liquid-air interface.

Centrifuging the L-BP suspension at 13,500 rpm (**Figure 1B**) led to the separation of dark yellow solid precipitate from light yellow supernatant (**Figure 1C**), which are identified as mainly nanosheets (denoted as L-BP-S) and nanoparticles (L-BP-P) by AFM (**Figures 1J** and **1K**), respectively. The thickness of *ca*. 93% of the nanosheets lies between 4.5 and 5.5 nm (70 flakes counted), representing 8 to 10 layers (*ca*. 0.53 nm per sheet [30]). Notably, such narrow thickness distribution is hardly achievable by using conventional LPE methods, which shows the great advantage of laser-assisted exfoliation. Beside flakes, a few particles (height = 5~8 nm) appear in the L-BP-S sample, while smaller particles (height = 2~5 nm) dominate the L-BP-P dispersion. The production of the particles commonly accompanies the laser interaction with the solid target in liquid and is explained by thermal evaporation mechanism:[31] the initial pulsed laser shots can generate a high-temperature plasma at the liquid-target interface, which

is quickly quenched by the surrounding solvent molecules, producing clustered particles with different sizes.[32]

2.2. Characterization of L-BP

The surface chemical state of the L-BP sample is compared with bulk BP by X-ray photoelectron spectroscopy (XPS). The survey spectra (**Figure S3**, SI) indicate the co-existence of P and O in both samples. The oxidation of P is inevitable due to the adsorption of oxygen and moisture on the sample surface: $P + O_2 \rightarrow P_xO_y + H_2O \rightarrow H_mPO_n$.[33] However, the P-to-O atomic ratio rises from 0.91 to 1.37 after irradiation, meaning the BP surface is reduced as a result of laser treatment. Such reduction is reasonable, considering that 2-propanol can serve as a reducing agent in the high-temperature environments induced by laser.

In the P 2*p* region shown in **Figure 2A**, bulk BP shows two intense peaks between 129 and 132 eV along with a broad peak between 132 and 136 eV. Deconvolution discloses four peaks in total at 129.8, 130.7, 133.7, and 134.8 eV, which can be assigned to the P $2p_{3/2}$ and P $2p_{1/2}$ of P-P bonding, O-P=O dangling bonding, and P_2O_5, respectively.[34] No significant change is observed after laser-treatment regarding the peak position of P $2p_{3/2}$ and P $2p_{1/2}$ apart from a 0.1 eV shift to the higher binding energy, suggesting that P-P bonding is retained after laser irradiation. The main difference is the areal ratio between unoxidized P in P-P bonding and oxidized P atoms, which increases from 2.3 in bulk BP to 4.6 in L-BP. Such a dramatic boost confirms that laser treatment can reduce the BP surface. Moreover, the slightly decreased ratio of P $2p_{3/2}$ over P $2p_{1/2}$ after laser-assisted exfoliation (from 1.78 of bulk BP to 1.43 of L-BP) suggests the creation of defects by irradiation.[34]

The O 1*s* region (**Figure 2B**) provides deeper insights into the oxidation state of BP. For bulk sample, the two peaks located at 531.8 and 533.0 eV can be assigned mainly to P=O and P-O-P bondings, respectively.[35] The P-O-P peak shifts to 532.4 eV after irradiation, which either

due to the change in chemical environments of bonded P or the formation of P-OH that was also observed by others.[34]

The X-ray powder diffraction (XRD) patterns of bulk BP, exfoliated BP nanosheets (L-BP-S), and BP nanoparticles (L-BP-P) are compared in **Figure 2C**. Both bulk BP and exfoliated BP show three distinctive peaks attributed to the (020), (040), and (060) crystallographic planes.[36] The disappearance of (021) plane after exfoliation implies that BP nanosheets are organized flatly on the SiO_2/Si substrate, in agreement with the AFM observation. Moreover, the declined peak intensity suggests the reduced crystalline size after exfoliation. Notably, the (020) diffraction peak shifts towards lower angle by 0.1°, an indication of enlarged *d* spacing, which can be reasoned with the variation of lattice strain due to layer number change. Compared to the nanosheets, the nanoparticles, L-BP-P, show minor diffraction peaks. Two aspects can contribute to such differences: the much smaller crystalline size of L-BP-P and possible amorphization caused by the laser.

The ultraviolet-visible (UV-vis) spectra describe the optical properties of L-BP (**Figure 2D**). As a semiconductor, L-BP suspension in 2-propanol exhibits strong adsorption from 200 to 600 nm, which agrees with the previous report.[37] Notably, the spectrum of L-BP turns out to be the mixed signal from nanosheets and nanoparticles. Like BP quantum dots,[38] the nanoparticle absorbs mainly the UV light, showing a sharp peak at 223 nm. On the contrary, BP nanosheet shows an extensive absorption within the visible light region up to 610 nm. The direct bandgap of BP nanosheet can be estimated by the Tauc analysis, shown as the inset in **Figure 2D**. An optical bandgap value of 2.7 eV is given, which is assigned to the high-energy band-to-band transition. For comparison, the high-energy transition energies are 1.95 eV and 3.15 eV for bulk and monolayer BP, respectively.[39] Such value usually is higher than the theoretical bandgap and often observed when using liquid suspension for UV-vis testing.[39-40]

Raman spectroscopy can provide a profound understanding of the BP structure, as already demonstrated by many researchers.[5, 41] **Figure 2E** compares the Raman spectra of bulk BP, L-BP-S, and L-BP-P using the Si peak at 520 nm for calibration. Three Raman peaks corresponding to A_g^1, B_g^2, and A_g^2 modes are identified at 357.6, 432.1, and 459.6 cm^{-1}, respectively.[42] The exfoliated BP nanosheets also show the three Raman peaks that are blue-shifted to higher values (for example, from 459.6 to 463.8 cm^{-1} for B_g^2 mode). Such peak-shifting is related to the number of BP layers and understood by the confined oscillation of P atoms as layer number increases.[43] The Raman spectrum of L-BP-P is quite different from bulk BP or L-BP-S, where a broad signal from 320 to 480 cm^{-1} and a distinguishable peak at 385.6 cm^{-1} are observed. Similar Raman profiles were reported in the literature, but with dissenting peak assignments. Some attributed the peak around 386 cm^{-1} to the P-O bonding,[35, 44] despite that the peak position matches neither P_2O_5 nor P_4O_{10}.[45] Moreover, recent studies on the oxidation mechanism of few-layer BP flakes indicated no additional peak formation within the Raman shift range of 320 to 480 nm.[15, 46] On the other hand, amorphous phosphorus shows a very similar Raman trait.[47] It is, therefore, reasonable to describe the L-BP-P nanoparticles as amorphous phosphorus, rather than the oxidized BP. The generation of the amorphous phase can be ascribed to the laser-induced rapid heating and quenching of BP plasma.

The ^{31}P magic angle spinning (MAS) solid-state nuclear magnetic resonance (ssNMR) is another powerful tool that can distinguish P-containing species within different chemical environments, including the crystalline and amorphous phases as well as its oxidized forms.[48] **Figure 2F** compares the ssNMR spectra of bulk BP, L-BP-S, and L-BP-P. For bulk BP, a dominating peak at the chemical shift of 15.1 ppm can be assigned to the P atoms in P-P environment of BP crystal, and the minor peaks at 2.3 and -6.9 ppm are owing to the H_mPO_n and P_xO_y, respectively, consistent with the literature.[33] After laser-assisted exfoliation, the

main peak of the nanosheet sample persists at 14.5 ppm, suggesting the structural stability of BP during laser-assisted exfoliation. Moreover, the linewidth of the peak shows no significant difference between exfoliated nanosheets and bulk crystals. Since the smaller linewidth indicates a more homogeneous ^{31}P chemical environment (thus higher crystallinity),[48] we can conclude that the laser treatment has a negligible effect on the atomic arrangement within BP nanosheets. Notably, the main peak shows a 0.6 ppm shift compared to that of bulk BP. This unexpected right-shifting representing the addition of P atom electron density in BP nanosheets after exfoliation is yet to be understood. Similarly, the oxidation of P to P_xO_y and further to H_mPO_n is minor compared to the primary P signal. The particle sample, on the other hand, shows a broad NMR signal from 20 to -10 ppm, an indication of dominating inhomogeneous/amorphous structure as well as partial oxidation. The possible formation of red phosphorus (RP) is ruled out since RP shows a broad signal between 100-0 ppm.[48] Thus, the particles should be amorphous BP, while the nanosheets are crystalline BP.

Also, it is worth mentioning that the nanoparticles, unlike the nanosheets, are highly unstable even under the protection of a deoxygenated liquid environment (color changes from yellow to colorless within two days). During the separation of its solid powder from the suspension in a glove box filled with Ar (O_2 level lower than 5 ppm), a small amount of white smoke (possibly P_2O_5 particles) was observed, demonstrating it is susceptible to oxidation.

2.3. Mechanism of laser-assisted exfoliation

Based on the characterizations and previous report[49] on laser-solid interaction, we propose a simplified mechanism for the laser-assisted exfoliation of bulk BP in **Figure 3** to better understand the processes. When a laser pulse interacts with the BP crystal in liquid (**Figure 3A**), a plasma is generated on the surface, together with minor clusters and fragments due to the impact. Featuring both ultra-high temperature and high pressure, the plasma has a typical duration in the range of a few ns to μs.[24] As the plasma decays, the energy is transferred to the

solvent molecules, which accelerates their movements and creates vapor bubbles around the plasma, as illustrated in **Figure 3B**. The severe expansion of the bubbles near the impact vacancies can enlarge the interlayer distance of BP. Meanwhile, the expansion-related shockwave travels in both parallel and perpendicular directions, further breaking the BP surface into small fragments (**Figure 3C**) while weakening the interlayer interaction. Finally, the generated few-layer BP flakes are rapidly quenched by the surrounding solvent (and reduced by the solvent in our experiment) and diffuse to the solution. Note that the production of nanoparticles accompanies the whole process since they are generated by the fast plasma quenching of ablated species.

However, the actual laser-solid interaction in the liquid is somewhat complicated, and the properties of the induced plasma (including volume, temperature, and lifetime, *etc.*) depend on several factors, such as laser duration, liquid environment, laser fluence, and wavelength.[50-52] Eventually, the morphology and structure of products are determined by these factors. For demonstration, we studied the effects of laser duration, energy, and solvent on the morphology and structure of BP exfoliated by the laser-assisted method.

2.4. Effect of laser duration

To analyze the duration effect, we shortened the irradiation time from previously used 4.8 μs (600 laser pulses) to 0.4 μs (50 pulses), 0.8 μs (100 pulses), and 2.4 μs (300 pulses). **Figures 4A** and **4B** show the typical TEM images of L-BP-S and L-BP-P after 2.4 μs of irradiation. In general, after irradiation, all L-BP samples contain both nanosheets (L-BP-S) and nanoparticles (L-BP-P), which can be separated after centrifuge. Notably, TEM images of the nanoparticles reveal a clear conversion from partially crystalline (**Figure 4C**) to a fully amorphous structure (**Figure 4D**) with prolonged irradiation time (from 0.4 to 2.4 μs), while no significant changes can be observed on the nanosheets. These findings agree with the previous characterization.

The concentration of the L-BP, including L-BP-S and L-BP-P, is determined by inductively coupled plasma optical emission spectroscopy (ICP-OES),[53] and illustrated in **Figure 4E**. As expected, the longer laser duration results in the higher L-BP concentration, showing a linear correlation from 0.22 mg mL^{-1} (0.4 μs) to 0.35 mg mL^{-1} (0.8 μs) and 0.74 mg mL^{-1} (2.4 μs) with a production rate of 0.25 mg mL^{-1} μs^{-1}. However, the L-BP concentration with 4.8 μs irradiation is lower (0.89 mg mL^{-1}) than expected. The individual contributions of nanosheets and nanoparticle to the total concentration can provide insights into the duration effect (right panel of **Figure 4E**). From 0.4 to 2.4 μs, the nanosheets are produced proportionally with a steady rate of 0.21 mg mL^{-1} μs^{-1}, while further irradiation cannot increase the concentration significantly. Conversely, the nanoparticles show a much lower but stable production rate of 0.04 mg mL^{-1} μs^{-1} within the studied duration.

Since the concentration information only provides the total P amount, the structure of the resulted nanosheets is studied to uncover the effect of laser duration. **Figure 4F** shows the AFM images of produced BP nanosheets with various laser durations. Height analysis reveals that the laser durations of 0.4 and 0.8 μs produce mainly BP flakes of 14 to 20 layers, while the prolonged irradiation of 2.4 and 4.8 μs generates the BP flakes with a layer number between 7 and 11 (reliability >80% from 70 counted flakes). With longer laser irradiation, the large unexfoliated chips disappear, indicating the exfoliation occurs gradually: thick flakes are formed initially and further exfoliated to thinner nanosheets. This mechanism can be explained by the secondary irradiation (**Figure 4K**) observed in Supplementary **Movie 1**: the initially created flakes diffuse to the solvent, and eventually into the path of the laser, causing secondary irradiation and further exfoliation of the flakes.

Such a correlation between the ablation duration and 2D material thickness is similar to that of sonication-assisted exfoliation, where a first-order kinetic process is proposed and the layer number decreases with a longer period.[54-55] However, the first-order relationship only applies

when the duration is shorter than 3 μs, as implied by **Figure 4E**. This is due to the difference between sonication ablation and laser ablation, where sonication can access the bulk materials from all directions while a laser can only access from one. Also, sonication energy is not affected by the presence of thinner chips in the suspension, but any particles can block laser energy on its path.

Figure 4G shows the Raman spectra of L-BP-S obtained at different duration. All samples show the three characteristic vibration modes. However, the Raman peaks shift to higher values with longer laser duration (middle panel of **Figure 4G**). As previously discussed, the shift of Raman peaks is closely related to the layer number of few-layer BP, and thinner nanosheets give greater peak shifts to high Raman shift, agreeing with the AFM observation.

Moreover, the A_g^1/A_g^2 ratio is an indicator of the oxidation levels of few-layer BP, and a value larger than 0.2 suggests low oxidation.[15] As shown in the right panel of **Figure 4G**, the A_g^1/A_g^2 ratio drops with laser irradiation time, from 0.90 (bulk BP) to *ca*. 0.74 (0.4~0.8 μs) and *ca*. 0.54 (2.4~4.8 μs), much higher than the 0.2 thresholds, suggesting the produced L-BP-S nanosheets are in low oxidation state. The decreasing correlation is caused by the laser treatment method since Martel *et al.* observed the opposite trend from the BP samples exfoliated by LPE.[15] However, the detailed mechanism is unclear and requires further work.

Figure 4H compares the Raman spectra of the nanoparticles obtained after different laser duration. At shorter irradiation times (0.4 and 0.8 μs), in addition to three vibrational modes of BP (with slight shifts, similar to the observation from BP quantum dots[38, 53]), the Raman peaks corresponding to amorphous phosphorus are evident at 385.6 and 352.1 cm^{-1} as well as broad signals between 400 and 480 cm^{-1}.[47] This indicates a mixed crystalline and amorphous phases in the nanoparticles produced in shorter durations, which echoes the mixed crystalline and amorphous atomic structure shown in **Figure 4C**. With longer irradiation, the three Raman modes of BP disappear, and the signals from the amorphous phase dominate the spectra (2.4

and 4.8 μs), a sign of full conversion of crystalline to amorphous phosphorus (**Figure 4D**). Unlike the nanosheets, different duration shows no significant influence on the height of the nanoparticles (2~6 nm for >90% particles from 150 counts of each sample). It is previously understood that the nanoparticles are generated *via* the rapid quenching of the laser-induced plasma by the solvent. Therefore, the laser duration (pulse counts) can affect the total population of nanoparticles, other than their size.

The effect of laser duration is proposed: the initial laser pulses can generate both few-layer BP nanosheets and nanoparticles. The concentrations of two products increase linearly with the laser duration (<2.4 μs). As the L-BP concentration rises to a certain level, secondary irradiation occurs (**Figure 4K**), which decreases laser fluence on the bulk BP target, thus fewer nanosheets can be produced, while still producing nanoparticles from the new target. The secondary irradiation also determines the structure and morphology of the products. For nanosheets, it causes further exfoliation of thicker flakes to thinner ones. While for nanoparticles, the irradiation results in the conversion from crystalline to the amorphous phase.

2.5. Effect of laser energy

The laser energy is limited by the total population of the photons (1.165 eV per photon), and low laser energy is expected to generate fewer L-BP products within the same duration. Since the production of both nanosheets and nanoparticles can be regarded as a first-order reaction within a period of 3 μs, we can compare the production rate of L-BP and L-BP-S at different laser energy, as shown in **Figure 4I**. A linear correlation between laser energy and the production rate is observed for both L-BP and L-BP-S. Such a trend shows a proportional relationship between the population of photons and the concentration of P atoms. The proposed mechanism is that a higher photon population leads to a higher impact probability of photons with BP targets, consequently more laser-induced shockwaves throughout the BP surface and more L-BP production.

Another significant impact of the laser energy caused to nanosheet product is the layer number, where higher power produces thinner flakes (7 ~ 14 layers with energy between 617 ~ 650 mJ while 18 ~ 25 layers with energy between 87 ~ 353 mJ). The dependence of layer number with laser energy is supported by the liquid state UV-vis spectra of L-BP-S suspension shown in **Figure 4J**. The peak intensity climbs with increasing laser energy and is consistent with the rising L-BP-S concentration. Meanwhile, the absorption edge shifts to a lower wavelength (red arrow), indicating a higher bandgap. Since thinner BP nanosheet shows higher bandgap,[39] higher laser energy can benefit thinner nanosheet production. This phenomenon can also be explained by the secondary irradiation illustrated in **Figure 4K**: the increased population of photons can increase the chance of an exfoliated nanosheet encountering other photons to spark further exfoliation.

2.6. Effect of solvent

The liquid environment is known to show significant impacts on the plasma lifetime and quenching process, and some solvent could react with the ablated species to reduce or oxidize the products.[24] We performed the laser-assisted exfoliation of BP in four solvents (hexane, methanol, ethanol, and 1-propanol), in addition to 2-propanol used in previous studies, to study the influence, using the same parameter set (laser duration = 4.8 μs, laser fluence = 2.59 J cm^{-2}). The produced L-BP was collected and redispersed in 2-propanol for AFM sample preparation to avoid different aggregation behaviors caused by solvents. Similar to the case of 2-propanol, the laser treatments in all four solvents produce both nanosheets and nanoparticles (AFM images of L-BP-S and L-BP-P shown in **Figures S4** and **S5**, SI). The nanosheets produced in 1-propanol and 2- propanol show the largest lateral size (> 5 μm), whereas the ones obtained in methanol (< 2 μm) and hexane (2~4 μm) are smaller in lateral size.

The significant difference lies in the thickness/height of the produced nanosheets and nanoparticles, as summarized in **Figure 5**. The nanosheets produced in alcohol solvents (**Figure**

5A, flake count > 70) show a narrow thickness distribution in the range of 8 to 13 layers, for example, 8~10 layers in 2-propanol and 11~12 layers in ethanol. The nanosheets exfoliated in hexane, however, are much thinner (3~5 layers). The surface roughness is another critical parameter when evaluating an exfoliation method, and it can affect the electronic properties of the nanosheets.[56] The arithmetic average of the absolute surface height (R_a) is measured on the surface of the nanosheets, and a higher R_a indicates the rougher surface (data in **Figure 5B**, examples in **Figure S6**, SI). The step regions between the BP nanosheets and SiO_2/Si substrate are avoided to reveal the information of only the nanosheet (inset of **Figure 5B**). Showing R_a < 3.0 nm, the surface of all nanosheets are quite smooth. Remarkably, hexane produces the nanosheets with the smallest height variation. Since the surface roughness is much lower after separating the L-BP-P nanoparticles from the L-BP-S nanosheets (**Figure S6,** SI), we believe the roughness originates mainly from the nanoparticles sitting on the top of nanosheets during AFM sample preparation. **Figure 5C** summarizes the aspect ratio (length/height, L/H) of nanosheets obtained in the five solvents, counting 20 flakes each. The length is defined as the diameter, shown in the inset of **Figure 5C**. Despite the high variation, the nanosheets prepared in 1-/2-propanol hold the highest aspect ratio >2000, while L-BP-$S_{methanol}$ shows the smallest value.

The mechanism of how liquid environment affects the lateral size and thickness (aspect ratio) of exfoliated BP nanosheets is not studied so far. A similar example of exfoliating graphite in different solvents reasoned that the H atoms generated by the plasma play a key role in stabilizing the exfoliated graphene, and the polar solvent molecules could provide electrical double layers protecting the products from restacking.[57] Such explanations were, however, commonly adopted to understand the laser-assisted production of nanoparticles with different sizes, not the production of layered materials.[31] Moreover, the XPS results show no sign of BP nanosheet functionalization by H atoms or solvent molecules. (**Figure S7**, SI)

To justify the solvent effect, we need to revisit the proposed mechanism in **Figure 3**, where the plasma causes both mechanical shockwaves across the BP crystal and high temperature in the localized region, inducing heat transfer from plasma to the solvent. The generation of solvent vapor bubbles is essential to overcome the van der Waals interaction. The thermal conductivity of the solvents follows the trend of hexane (0.120 W m^{-1} K^{-1}) < 2-propanol (0.135 W m^{-1} K^{-1}) < 1-propanol (0.154 W m^{-1} K^{-1}) < ethanol (0.169 W m^{-1} K^{-1}) < methanol (0.200 W m^{-1} K^{-1}),[58] making it easier to generate the localized hexane bubbles upon the heat transfers from BP. Besides, the non-polar nature of hexane may also contribute to the production of thinner nanosheets than in other polar solvents. Because the P-P bonding in BP crystal is also non-polar, such a difference in solvent polarity can affect the BP-solvent interaction. However, the precise interpretation of the solvent effect requires more controlled experiments and advanced in situ instrumental characterizations, as well as theoretical simulations.

The nanoparticles, on the other hand, can be found in the precipitate as well as the supernatant after centrifugation. Shown in **Figure 5D**, the height of the nanoparticles in the supernatant ranges from 2 to 20 nm. Since they are not crystalline BP anymore, it is meaningless to calculate the layer number based on BP structure. The nanoparticles generated in 1-propanol, 2-propanol, and hexane show a similar height between 2 and 5 nm, while average heights of 5.6 and 15.3 nm are suggested for those fabricated in ethanol and methanol, respectively.

2.7. Morphologic effect of BP nanosheets as the anode of LIBs

BP is one of the most promising anode materials for LIBs. During the charge/discharge process, thanks to the stacking structure of BP, Li^+ ions can transfer throughout the interlayer space (**Figure 6A**). Full discharge produces Li_3P, showing a theoretical capacity of 2596 mAh g^{-1}.[11] However, bulk BP has poor stability (83% capacity loss from 1279 to 220 mAh g^{-1} after 30 charge/discharge cycles), slow Li^+ ion diffusion (long diffusion path), as well as low electronic conductivity due to its characteristics as a semiconductor.[9] The instability is attributed mainly

to the structural deformation (277% volume expansion from BP to Li_3P)[59] caused by lithiation. One common strategy to reduce the impact of volume expansion is to use the 2D analog, as demonstrated in other 2D materials,[54, 60-61] which can also significantly shorten the diffusion path for ions and enlarge the surface area. Recently, both theoretical and experimental results demonstrated that exfoliating BP to its few-layer form could improve the anode stability.[10, 62-63] Still, the influence of the BP thickness and lateral size on the LIBs performance remains unknown, mainly owing to the lack of scalable and thickness-controlled exfoliation methods. Laser-assisted exfoliation, as previously demonstrated, enables the production of BP nanosheets with narrow thickness distribution. To highlight the effects of thickness/lateral size on the LIB performances, we tested the as-prepared few-layer BP nanosheet samples (4.8 μs irradiation) obtained in three different solvents (hexane, 2-propanol, and methanol) against a Li foil in a CR2032 half-cell configuration (**Figure 6A**, see the experimental section for details), denoted as L-BP-S_{hexane}, L-BP-$S_{2\text{-propanol}}$, and L-BP-$S_{methanol}$, respectively. As shown by **Figures 5** and **S5**, the layer number follows a trend of L-BP-S_{hexane}(3~5) < L-BP-$S_{2\text{-propanol}}$(8~10) ≈ L-BP-$S_{methanol}$(8~10), while the lateral size showing L-BP-$S_{methanol}$(< 2 μm) < L-BP-S_{hexane}(2~4 μm) < L-BP-$S_{2\text{-propanol}}$(> 5 μm). However, BP nanosheet has a larger bandgap than its bulk form, meaning even more reduced conductivity. The current solution for addressing this drawback is to involve conductive additives such as graphite and carbon paper to form C-O-P bonding.[10, 59] Therefore, to study the morphological effect of BP nanosheets without significant structural changes, we physically mixed the L-BP-S nanosheets suspension with conductive carbon (commercial Super P) powder (mass ratio 2:1) to increase the conductivity. As a result, the theoretical capacity of the few-layer BP/C composite is 1854 mAh g^{-1} (66.7% × theoretical capacity of BP + 33.3% × theoretical capacity of carbon). The specific capacity data of BP is normalized to the weight of BP in the following discussion.

Figure 6B compares the first cyclic voltammograms (CVs) of the three LIBs at a rate of 0.03 mV s^{-1} to highlight the Li^+ ion transfer process. All L-BP-S anodes show minor current signal when discharging from 3.0 to 1.5 V, which is the reduction current of the oxidized P species. During the discharge process from 1.5 to 0.5 V (*vs.* Li^+/Li), a broad signal evolves for both L-BP-S_{hexane} and L-BP-$S_{methanol}$, while multiple peaks emerge for L-BP-$S_{2\text{-propanol}}$. The peaks in this potential window are assigned to the lithiation: BP → Li_2P.[9] Further discharging the half-cell from 0.5 to 0.001 V reveals a stabling current signal known as the formation of Li_3P. The main difference between the L-BP-S samples lies in the Li_xP formation region, as highlighted in **Figure 6B**. The broad peak of both L-BP-S_{hexane} and L-BP-$S_{methanol}$ suggests one-step Li_2P formation (the peak at 0.80 V) without involving distinctive multiple lithiation processes (BP → Li_xP ($0 < x < 1$) → LiP → Li_2P). However, L-BP-$S_{2\text{-propanol}}$ anode shows the well-defined peaks at 1.18 and 0.76 V. The difference can be addressed by the structure: the Li^+ diffusion distance in L-BP-S_{hexane} (lowest layer number) and L-BP-$S_{methanol}$ (smallest lateral size) are reasonably shorter than that in L-BP-$S_{2\text{-propanol}}$ (similar thickness to L-BP-$S_{methanol}$ but larger lateral size). Unlike the discharge signal, the charging current response of the electrodes is similar. The sharp peak at *ca*. 0.15 V and the broad peak between 0.62 and 1.50 V are related to the Li_3P → Li_2P and Li_2P → BP processes, respectively.

We further analyzed the charge/discharge voltage profiles of the L-BP-S electrodes during the first (**Figure S8**, SI), 50th, 100th, 150th, and 200th (**Figure 6C**) galvanostatic cycle in the potential range of 0.001 to 3.0 V at a current density of 1.0 A g^{-1}, separately. The initial charge/discharge capacities of L-BP-S_{hexane}, L-BP-$S_{methanol}$, and L-BP-$S_{2\text{-propanol}}$ electrodes are 441.1/1111.0, 495.6/1263.0, and 535.0/1161.4 mAh g^{-1}, representing a Coulombic efficiency of 40.2 %, 39.2 %, and 46.1 %, respectively, for the first cycle. These results display large irreversible capacities, which are commonly observed during the first cycle using BP as the

anode material.[9, 11, 64] Such initial loss is caused mainly by the formation of solid-electrolyte interphase (SEI) film from the decomposition of electrolyte solvents at the electrode/electrolyte interface.[65] Further charge/discharge profiles at higher cycle numbers (**Figure 6C**) show much higher Coulombic efficiencies (>99% for all), indicating a stable interface has formed. During the charge (delithiation) and discharge (lithiation), two voltage plateaus are evident at *ca.*0.75 and 0.30 V for all L-BP-S samples, which are ascribed to the BP → Li_xP and Li_xP → Li_3P ($0 < x \leq 2$). Notably, L-BP-S_{hexane} shows the fastest potential drop from 3.0 to 1.2 V, followed by L-BP-$S_{2\text{-propanol}}$ and L-BP-$S_{methanol}$. Since the potential can be understood as the driving force to push/pull Li^+ ion out/in the BP structure during delithiation and lithiation, the faster potential drop suggests more homogeneous Li^+ distribution in L-BP-S_{hexane} than in L-BP-$S_{2\text{-propanol}}$ and L-BP-$S_{methanol}$ where high voltage activations are required to remove/gain some Li^+ ions.

Figure 6D shows the rate capability of each electrode at the variety of current densities ranging from 0.2 to 5.0 A g^{-1} to demonstrate the electrochemical properties of each electrode during a considerably fast redox reaction.[60] At a relatively low current density of 0.2 A g^{-1} where the complete delithiation/lithiation are allowed regardless the diffusion rate of Li^+ ions, the three electrodes show the similar specific capacity of *ca.* 510 mAh g^{-1} after the formation of stable SEI layer, which is also comparable with other reported BP anodes (a comparison table is shown as **Table S1**, SI).[64, 66-67] Higher current density reveals the kinetic difference of delithiation/lithiation in L-BP-S electrodes. Among the samples investigated, L-BP-S_{hexane} electrode shows the highest specific capacity of 305.7 mAh g^{-1} at 3.0 A g^{-1} and 273.6 mAh g^{-1} at a high current density of 5 A g^{-1}, while those values are 254.0 (3.0 A g^{-1})/232.6 mAh g^{-1}(5.0 A g^{-1}) for L-BP-$S_{2\text{-propanol}}$ and 181.1 (3.0 A g^{-1})/161.6 mAh g^{-1}(5.0 A g^{-1}) for L-BP-$S_{methanol.}$ The capacity at high current density suggests the delithiation/lithiation rate follows the trend of L-BP-S_{hexane} > L-BP-$S_{2\text{-propanol}}$ > L-BP-$S_{methanol}$. After the rate capability test at 5.0 A g^{-1}, the cells were tested again at 0.2 A g^{-1}. L-BP-S_{hexane} electrode shows a well-recovered capacity of 529.9

mAh g^{-1} (3.9 % increase), comparing to 432.0 mAh g^{-1} (15.3 % loss) of L-BP-$S_{2\text{-propanol}}$ and 305.7 mAh g^{-1} (40.1 % loss) of L-BP-$S_{methanol}$. The capacity fade is generally believed to be related to the loss of Li^+ and/or SEI formation at high current density.[68] Therefore, based on the voltage profiles and rate capability test, the L-BP-S_{hexane} electrode demonstrates the fastest and more complete delithiation/lithiation among the three electrodes. To confirm the long-term cycling stability, the cycle performances of L-BP-S electrodes are tested for 200 cycles at the current density of 1.0 A g^{-1} (**Figure 6E**). The L-BP-S_{hexane}, L-BP-$S_{methanol}$, and L-BP-$S_{2\text{-propanol}}$ electrodes show very stable cyclability and high specific capacities of 404.4, 340.4, and 307.4 mAh g^{-1} after 200 cycles, respectively, which indicates the structural stability of laser-assisted exfoliated BP nanosheets.

To gain a deeper understanding of the kinetic difference of delithiation/lithiation in L-BP-S electrodes and to identify the Li^+ ion diffusion effect and charge transfer resistance effect, we employed the galvanostatic electrochemical impedance spectroscopy (GEIS). The LIBs were cycled 10 times at 0.2 A g^{-1} to stabilize the SEI layer before acquiring GEIS at the open-circuit voltage (OCV). **Figure 6F** shows the corresponding Nyquist plots. All spectra reveal a depressed semicircle at the high/medium-frequency domain and an inclined line at the low-frequency domain. The data can be fitted with the equivalent circuit shown in the inset of **Figure 6F**, featuring an uncompensated resistance (R_s), a surface and interfacial charge transfer resistance (R_c), a constant phase element (CPE), and a Warburg impedance (W, due to the depressed shape).[69]

All cells show R_s of *ca.* 1.2 **Ω**, ensuring the proper cell assembly. The significant difference lies in the R_c (**Figure 6G**), an indicator of electronic conductivity at the electrolyte-electrode interface. The L-BP-S_{hexane} electrode owns the smallest resistance of 253 **Ω**, followed by L-BP-$S_{2\text{-propanol}}$ (297 **Ω**) and L-BP-$S_{methanol}$ (426 **Ω**). The resistance difference can be reasoned with the electron transfer path in the BP/C composite, as illustrated in **Figure 6H**. Since L-BP-S_{hexane}

has the lowest layer number, the electron transfer path to cover the whole nanosheet is the shortest, thus gives the smallest charge transfer resistance. L-BP-$S_{2\text{-propanol}}$ and L-BP-$S_{methanol}$ have a similar layer number but L-BP-$S_{2\text{-propanol}}$ shows a more significant aspect ratio (**Figure 5C**). As a result, the electron transfer along the 2D layer is much improved by the higher crystallinity in larger BP flakes, compared with the multiple interfaces of BP-carbon-BP in the L-BP-$S_{methanol}$ electrode. Moreover, the highest surface roughness of the L-BP-$S_{methanol}$ can contribute to the reduced electron transfer between BP flakes and carbon particles.

The Li^+ ion diffusion coefficient *D* is inversely proportional to σ^2, where σ is the Warburg coefficient (shown in **Figure 6G**) calculated by plotting Z_{re} against the reciprocal root square of the lower angular frequencies ($\omega^{-0.5}$, **Figure S9**, SI). Therefore, the Li^+ ion diffusion coefficient in L-BP-S_{hexane} is 1.3 and 2.0 times higher than in L-BP-$S_{methanol}$ and L-BP-$S_{2\text{-propanol}}$, respectively. Such results are reasonable as L-BP-S_{hexane} nanosheets are the thinnest while having a reasonably low aspect ratio to shorten the diffusion path. As to nanosheets of similar thickness, the low aspect ratio allows more edge regions, facilitating the Li^+ diffusion.

Based on the above analysis, it is suggested that a low layer number is beneficial to both charge transfer and Li^+ ion diffusion, while a high aspect ratio can improve the charge transfer but may increase the Li^+ ion diffusion path and hinder the delithiation/lithiation processes.

The morphology of the anode surface before and after 200 cycles are compared in **Figure S10** by their scanning electron microscopic (SEM) images and the corresponding elementary mapping of carbon and phosphorus. Before cycling, the even distributions of C and P indicate the complete and uniform mixture of carbon black and BP flakes. Notably, L-BP-S_{hexane} electrode shows the roughest surface (porous structure), followed by L-BP-$S_{methanol}$ and L-BP-$S_{2\text{-propanol}}$ electrodes. After 200 cycles, the L-BP-S_{hexane} electrode shows little morphological difference, while a polymer-like SEI layer is observed from the others. These visible formation of SEI layer on both L-BP-$S_{methanol}$ and L-BP-$S_{2\text{-propanol}}$ electrodes matches the previous rate

capability results that thinner BP nanosheets can benefit the Li^+ ion transfer and prevent the SEI layer formation at high current density.

2.8. L-BP/graphene composite as the anode of LIBs

In order to prevent interference, no optimization of the material was made in the above study. Considering that L-BP-S_{hexane} has the best performance, we tried to further unleash the potential of the L-BP-S_{hexane} nanosheets by involving graphene as an ingredient, a common method that has been proved beneficial for increasing the stability of few-layer BP.[10, 70] Both half-cell and full-cell configurations were studied.

Figure 7A shows the half-cell voltage profiles of L-BP-S_{hexane}/graphene anode with a specific capacity of 2217 mAh g^{-1} in the first cycle, and 970 mAh g^{-1} after 75 cycles, which are much higher than bare L-BP-S_{hexane}. The capacity boost can be attributed to the stability improvement of few-layer BP by the introduction of graphene, which has been discussed in detail elsewhere.[10, 70]

The pre-lithiated BP half-cells were opened and re-assembled into full-cell configuration using lithium iron phosphate (LFP) as the cathode (L-BP-S_{hexane}/graphene||LFP). The performance was shown in **Figures 7B** and **7C**. The contribution from graphene to the cell capacity is negligible (< 10 mAh g^{-1}), as shown in **Figure S11**. The first cycle of the full-cell shows a discharge capacity of 1084 mAh g^{-1}, and the 100th cycle indicates 247 mAh g^{-1}, with a coulombic efficiency of 92%. After the initial undulation caused by structural perturbation to BP-based anode after cell opening and assembly, the full-cell reaches stable charge/discharge cycles after 20 cycles, demonstrating the possibility of using BP-based anode in the full-cells.

The post-test cross-sectional SEM image of the L-BP-S_{hexane}/graphene anode was compared to its pristine form in **Figure 7D**, where the thickness has grown from 11.6 to 13.5 μm, a sign of the SEI layer formation (related elemental mappings of the SEM images in **Figure S12**). No other deformation of the anode layer were observed, suggesting its high stability.

Finally, the volumetric energy density of the full-cell was shown by **Figure 7E** (calculation is shown in supporting information).[71] Despite the low BP amount we applied in the full-cell, a comparable high energy density of 432 Wh L^{-1} was demonstrated in the initial cycles, and stable value of 119 Wh L^{-1} was established after 50 cycles. By increasing the BP loading, we believe that the energy density of BP-based full-cell can be further lifted.

Comparing the half-cell and full-cell (**Figures 7A** and **7B**), we expect the capacity loss is mainly caused by the oxidation of BP-based anodes during the assembly as well as the structural evolution after cycling as half-cells. Therefore, more work is required to establish a procedure for BP-based anode treatment.

3. Conclusion

To conclude, we demonstrated a pulsed laser-assisted exfoliation method to produce few-layer BP nanosheets in a swift and controllable manner. By changing the irradiation time, energy, and solvent type, the morphology (thickness and lateral size) and structure of as-prepared BP nanosheets can be altered. Longer laser irradiation and higher energy promote the exfoliation to thinner BP flakes (7~11 layers after 4.8 μs) at a higher yield, but at the cost of structural change from crystalline to amorphous. Phosphorus nanoparticles (diameter = 2 ~ 8 nm) are also produced as a byproduct, which can be separated easily from the nanosheets *via* centrifuge. Prolonged laser irradiation results in the phase transition of crystalline nanoparticles to its amorphous form. The solvent environment also affects the properties of exfoliated BP in terms of thickness and lateral size. In alcohol solvents, the nanosheets show a narrow thickness distribution of 8 to 13 layers, increasing from 8~10 layers in 2-propanol to 11~12 layers in ethanol. A much thinner (3~5 layers) BP flakes with smaller lateral size (< 2~4 μm) is obtained in hexane. Moreover, when exfoliated in the alcohol solvent, such as 2-propanol, the BP nanosheets are reduced, compared to bulk BP crystal, which is beneficial for maintaining structural integrity.

The production of BP nanosheets and nanoparticles is understood by a simplified mechanism, which involves the rapid quenching of the laser-induced BP plasma on the BP crystal surface by surrounding solvent molecules. The generation of vapor bubbles after energy transfer facilitates the weakening of interlayer van der Waals interaction to produce nanosheets, which can be further exfoliated by secondary irradiation. Meanwhile, quenching of the clusters in the plasma promotes the nanoparticle production.

Using the thickness- and lateral size-controlled BP nanosheets as the anode for LIBs provides insights into the morphological and structural impact on BP-based anode performance. All BP nanosheets exfoliated by laser show high stability without noticeable capacity fade within 200 cycles. Specifically, a low layer number is beneficial to both charge transfer and Li^+ ion diffusion, while the larger lateral size can improve the charge transfer but at the cost of longer Li^+ ion diffusion path and thus slower delithiation/lithiation.

Moreover, after forming a composite with graphene, the BP/graphene anode shows a stable specific capacity of 970 mAh g^{-1} in half-cell and 247 mAh g^{-1} in full-cell configurations, exhibiting stable energy density of 119 Wh L^{-1}.

The laser-assisted exfoliation method could offer an excellent alternative path towards the controlled exfoliation of other 2D materials, which significantly impact the performance of energy conversion and storage applications.

4. Experimental Section

Materials. The BP crystal was prepared *via* chemical vapor transport (CVT). Hexane, methanol, ethanol, 1-propanol, and 2-propanol were purchased from Sigma-Aldrich with purity ≥99%. The solvents were bubbled with Ar for 10 min before laser treatment to remove dissolved oxygen. For battery assembly, copper foil, N-methyl-2-pyrrolidone (NMP), conductive carbon black (TIMCAL graphite & carbon Super P), and PVdF (HSV900) were purchased from MTI.

The electrolyte (1 M $LiPF_6$ in the 1:1 mixed solvent of ethylene carbonate and diethyl carbonate) was obtained from DodoChem.

Laser-assisted exfoliation. The Nd:YAG Q-switched pulsed laser (Nimma-600 Laser system) is provided by Beamtech Optronics Co.Ltd with an energy output of 650 mJ and energy stability (RMS) ≤1%. The beam diameter is ~8 mm. The liquid column height between the BP target and the liquid surface is 3 cm. Before laser treatment, the sample chamber is filled with Ar to remove oxygen. The energy attenuation of the laser is achieved by adjusting the laser angle. Due to safety concerns of laser and potential P-related compounds, a mask and a protection goggle are required during the whole process.

Material characterization. The AFM images were taken on a Bruker Multimode 8 HR system using the PeakForce Tapping mode with SNL-10 cantilever (silicon tip on nitride lever, k = 0.12 N m^{-1}). The setpoint of all imaging was 0.1 to validate the thickness comparison from different images. The AFM samples were prepared by drop-casting the suspension onto the ultra-flat thermal SiO_2/Si substrates (Ted Pella, Inc.) and dried within a solvent-saturated enclosure to slow the evaporation process while preventing O_2/H_2O adsorption. For L-BP prepared in 2-propanol, the suspension was diluted to 0.01 mg mL^{-1} before drop-casting. For L-BP obtained in other solvents, the solvents were removed by rotary evaporator at 40 °C, and the product was dispersed in 2-propanol with the same concentration of 0.01 mg mL^{-1}. All samples were tested immediately after preparation.

The TEM imaging was performed on a JEOL system (Model JEM-2100F, 200 kV). The samples were prepared by drop-casting the suspension (~0.05 mg mL^{-1}) on carbon-coated copper grids, and excess fluid was removed by a filter paper. The prepared samples were characterized immediately after drying. During the imaging process, no significant lattice change was observed at the operation voltage (200 kV). The SEM imaging was carried out on a TESCAN MAIA3 system.

The XPS spectra were acquired using a Thermo Fisher ESCALAB 250Xi system. 100 μL of the suspension (0.5 mg mL^{-1}) was drop-cast on a thermal SiO_2 substrate and allowed to dry in the glovebox (Mbraun) overnight. The spectrometer was calibrated using the C 1*s* peak at 284.6 eV. The data were fitted with CasaXPS software, using a Spline Shirley type background and peak profile of Gaussian-Lorentzian GL(30).

The total phosphorus concentration of all samples was measured using the ICP-OES (Agilent 710 Series). All samples were dispersed in 2-propanol and diluted to its 10% concentration. The plasma was generated using argon and compressed air to reduce the carbon emission caused by the 2-propanol solvent. The flow rate of plasma was 18 L min^{-1} for all testing, and the wavelength of 214.912 nm was selected.

The UV-vis spectroscopy was carried out using an AvaLight UV/Vis/NIR light source with an AvaSpex-UL S2048 Fiber-Optic spectrometer. The samples were diluted in 2-propanol and tested using a quartz cuvette.

The Raman spectra were obtained from a Witec confocal Raman system (alpha300 R). The excitation laser (λ = 532 nm) energy was 5 mW for all tests to avoid potential heat damage of samples. The sampling of all flakes was carried out at a low-frequency in the central region of the sheets.

The ^{31}P magic angle spinning (MAS) nuclear magnetic resonance (NMR) spectra were obtained from a Jeol ECZ500R 500 MHz Solid-state NMR spectrometer under room temperature. For sample preparation, the as-prepared L-BP-P and L-BP-S were mixed with Super P carbon with a mass ratio of 1:5 for sample dilution. The BP crystal was used directly for the NMR test. The samples were packed into a 4 mm diameter cylindrical zirconia rotor in a glove box filled with Ar to avoid oxidation of BP samples. The spinning speed of all experiments was 10 kHz.

The X-ray powder diffraction (XRD) characterization was finished using a SmartLab X-ray diffractometer by Rigaku (voltage 45 kV, current 200 mA). The samples were prepared by

drop-casting the concentrated suspension onto the ultra-flat thermal SiO_2/Si substrates (Ted Pella, Inc.), followed by drying in the glove box with Ar filling.

Half-cell LIB assembly. The L-BP-S dispersion was dried and mixed with the conducting material (Super P) and the binder agent (PVdF) in NMP with a mass ratio of 6:3:1 in a glovebox (Mbraun, Ar atmosphere). After well-mixing with a mortar for 30 min, the as-obtained slurry was cast on a copper foil by using a doctor blade and dried on a hot plate under 60 °C for 24 h in the glovebox. The total amount of L-BP-S on each foil was ~0.20 mg cm^{-2}. A glass fiber separator (Watman GF/C) and Li metal film as a counter electrode were used to assemble the coin-type cells (CR2032) in an Ar-filled glove box. The 50 μL of electrolyte used was 1 M $LiPF_6$ in the mixed solvent of ethylene carbonate and diethyl carbonate (EC and DEC with a volume ratio of 1:1). For L-BP-S/graphene composite, the mass ratio between L-BP-S and graphene (XFNANO, China) was 2:1, and the BP per cell was ~0.20 mg cm^{-2}.

Full-cell LIB assembly. For a typical assembly of CR2032 full cell, the $LiFePO_4$ (LFP) cathodes were prepared by coating a slurry ($LiFePO_4$:super P carbon:PVDF = 8:1:1) on pure Al foil, followed by drying under vacuum at 60 °C overnight. The mass loading of the cathode was ~2.2 mg cm^{-2} (1.4 times of BP based on the real capacity). The BP-based anode was first assembled to a half-cell with Li metal for pre-lithiation and subjected to the discharging process to achieve a stable Li^+-BP structure at the current density of 50 mA g^{-1} until 50 mV. The pre-lithiation BP-based anode was then opened and re-assembled into a full-cell with as-prepared LFP cathode, which was precisely pairing with anode.

LIB test. The GEIS and CV results of batteries were obtained on a PARSTAT MC (PMC1000/DC) electrochemical system (Princeton Applied Research, USA). Before the test, the cells were allowed to rest for 24 hours to reach an OCV higher than 2.50 V. The frequency range for GEIS tests was 10 mHz to 100 kHz with an amplitude current of 0.5 mA RMS (root mean square). CV tests were conducted in the potential range between 0.001 and 3.0 V at a scan

rate of 0.03 mV s^{-1}. The charge/discharge cycling evaluation of the half-cells was tested on a WonATech battery testing system (WBCS3000L) in the range of 0.001 to 3.0 V. The full-cells were tested at the current density of 100 mA g^{-1} in the potential range between 1.5 and 3.7 V.

Supporting Information

Supporting Information (SI) is available from the Wiley Online Library or the author. SI includes laser setup, video clip of laser treatment process, AFM sample preparation, XPS spectra, AFM images, surface roughness measurements, voltage profiles, LIB performance comparison, SEM images (mapping), graphene||LFP full-cell test results, and calculation details.

Acknowledgements

This work was supported by the Innovation and Technology Commission of Hong Kong and the Hong Kong Polytechnic University (grant number 1-BE0Y). We gratefully acknowledge the support of the University Research Facility on Chemical and Environmental Analysis (UCEA) of the Hong Kong Polytechnic University for the ^{31}P solid-state NMR test.

† These authors contributed equally.

Received: ((will be filled in by the editorial staff))
Revised: ((will be filled in by the editorial staff))
Published online: ((will be filled in by the editorial staff))

References

[1] F. Xia, H. Wang, J. C. M. Hwang, A. H. C. Neto, L. Yang, *Nat. Rev. Phys.* **2019**, 1, 306.
[2] X. Yan, H. Wang, I. Sanchez Esqueda, *Nano Lett.* **2019**, 19, 482.
[3] R. Gusmao, Z. Sofer, M. Pumera, *Angew. Chem. Int. Ed.* **2017**, 56, 8052.
[4] Y. Zhang, Y. Zheng, K. Rui, H. H. Hng, K. Hippalgaonkar, J. Xu, W. Sun, J. Zhu, Q. Yan, W. Huang, *Small* **2017**, 13, 1700661.
[5] F. Xia, H. Wang, Y. Jia, *Nat. Commun.* **2014**, 5, 4458.
[6] S. Lin, Y. Li, J. Qian, S. P. Lau, *Mater. Today Energy* **2019**, 12, 1.
[7] S. Wu, K. S. Hui, K. N. Hui, *Adv. Sci.* **2018**, 5, 1700491.
[8] J. Ni, L. Li, J. Lu, *ACS Energy Lett.* **2018**, 3, 1137.
[9] C. M. Park, H. J. Sohn, *Adv. Mater.* **2007**, 19, 2465.
[10] L. Chen, G. Zhou, Z. Liu, X. Ma, J. Chen, Z. Zhang, X. Ma, F. Li, H. M. Cheng, W. Ren, *Adv. Mater.* **2016**, 28, 510.
[11] L.-Q. Sun, M.-J. Li, K. Sun, S.-H. Yu, R.-S. Wang, H.-M. Xie, *J. Phys. Chem. C* **2012**, 116, 14772.
[12] J. L. Zhang, C. Han, Z. Hu, L. Wang, L. Liu, A. T. S. Wee, W. Chen, *Adv. Mater.* **2018**, 30, e1802207.
[13] V. Nicolosi, M. Chhowalla, M. G. Kanatzidis, M. S. Strano, J. N. Coleman, *Science* **2013**, 340, 1226419.

[14] S. Lin, Y. Chui, Y. Li, S. P. Lau, *FlatChem* **2017**, 2, 15.
[15] A. Favron, E. Gaufres, F. Fossard, A. L. Phaneuf-L'Heureux, N. Y. Tang, P. L. Levesque, A. Loiseau, R. Leonelli, S. Francoeur, R. Martel, *Nat. Mater.* **2015**, 14, 826.
[16] P. Yasaei, B. Kumar, T. Foroozan, C. Wang, M. Asadi, D. Tuschel, J. E. Indacochea, R. F. Klie, A. Salehi-Khojin, *Adv. Mater.* **2015**, 27, 1887.
[17] D. Hanlon, C. Backes, E. Doherty, C. S. Cucinotta, N. C. Berner, C. Boland, K. Lee, A. Harvey, P. Lynch, Z. Gholamvand, S. Zhang, K. Wang, G. Moynihan, A. Pokle, Q. M. Ramasse, N. McEvoy, W. J. Blau, J. Wang, G. Abellan, F. Hauke, A. Hirsch, S. Sanvito, D. D. O'Regan, G. S. Duesberg, V. Nicolosi, J. N. Coleman, *Nat. Commun.* **2015**, 6, 8563.
[18] W. Zhao, Z. Xue, J. Wang, J. Jiang, X. Zhao, T. Mu, *ACS Appl. Mater. Interfaces* **2015**, 7, 27608.
[19] J. Kang, S. A. Wells, J. D. Wood, J. H. Lee, X. Liu, C. R. Ryder, J. Zhu, J. R. Guest, C. A. Husko, M. C. Hersam, *Proc. Natl. Acad. Sci. U. S. A.* **2016**, 113, 11688.
[20] M. Qian, Y. S. Zhou, Y. Gao, J. B. Park, T. Feng, S. M. Huang, Z. Sun, L. Jiang, Y. F. Lu, *Appl. Phys. Lett.* **2011**, 98, 173108.
[21] M. Jalili, H. Ghanbari, S. Moemen Bellah, R. Malekfar, *J. Mater. Sci. Technol.* **2019**, 35, 292.
[22] M. Qian, Y. S. Zhou, Y. Gao, T. Feng, Z. Sun, L. Jiang, Y. F. Lu, *Appl. Surf. Sci.* **2012**, 258, 9092.
[23] G. Carotenuto, A. Longo, L. Nicolais, S. De Nicola, E. Pugliese, M. Ciofini, M. Locatelli, A. Lapucci, R. Meucci, *J. Phys. Chem. C* **2015**, 119, 15942.
[24] D. Zhang, B. Gokce, S. Barcikowski, *Chem. Rev.* **2017**, 117, 3990.
[25] S. R. Suryawanshi, M. A. More, D. J. Late, *RSC Adv.* **2016**, 6, 112103.
[26] H. Huang, J. Li, Y. Yi, J. Wang, Y. Kang, P. K. Chu, H. C. Ong, X. F. Yu, *Chem. Commun.* **2018**, 54, 2365.
[27] A. Castellanos-Gomez, L. Vicarelli, E. Prada, J. O. Island, K. L. Narasimha-Acharya, S. I. Blanter, D. J. Groenendijk, M. Buscema, G. A. Steele, J. V. Alvarez, H. W. Zandbergen, J. J. Palacios, H. S. J. van der Zant, *2D Mater.* **2014**, 1, 025001.
[28] T. P. Bigioni, X. M. Lin, T. T. Nguyen, E. I. Corwin, T. A. Witten, H. M. Jaeger, *Nat. Mater.* **2006**, 5, 265.
[29] Q. Wang, J. Qian, Y. Li, Y. Zhang, D. He, S. Jiang, Y. Wang, X. Wang, L. Pan, J. Wang, X. Wang, Z. Hu, H. Nan, Z. Ni, Y. Zheng, Y. Shi, *Adv. Funct. Mater.* **2016**, 26, 3191.
[30] R. Hultgren, N. S. Gingrich, B. E. Warren, *J. Chem. Phys.* **1935**, 3, 351.
[31] H. B. Zeng, X. W. Du, S. C. Singh, S. A. Kulinich, S. K. Yang, J. P. He, W. P. Cai, *Adv. Funct. Mater.* **2012**, 22, 1333.
[32] A. Letzel, B. Gökce, P. Wagener, S. Ibrahimkutty, A. Menzel, A. Plech, S. Barcikowski, *J. Phys. Chem. C* **2017**, 121, 5356.
[33] Y. Wang, B. Yang, B. Wan, X. Xi, Z. Zeng, E. Liu, G. Wu, Z. Liu, W. Wang, *2D Mater.* **2016**, 3, 035025.
[34] X. Zhu, T. Zhang, Z. Sun, H. Chen, J. Guan, X. Chen, H. Ji, P. Du, S. Yang, *Adv. Mater.* **2017**, 29, 1605776.
[35] B. Tian, B. Tian, B. Smith, M. C. Scott, Q. Lei, R. Hua, Y. Tian, Y. Liu, *Proc. Natl. Acad. Sci. U. S. A.* **2018**, 115, 4345.
[36] C. Hao, B. Yang, F. Wen, J. Xiang, L. Li, W. Wang, Z. Zeng, B. Xu, Z. Zhao, Z. Liu, Y. Tian, *Adv. Mater.* **2016**, 28, 3194.
[37] X. Ren, Z. Li, Z. Huang, D. Sang, H. Qiao, X. Qi, J. Li, J. Zhong, H. Zhang, *Adv. Funct. Mater.* **2017**, 27, 1606834.
[38] Y. H. Xu, Z. T. Wang, Z. N. Guo, H. Huang, Q. L. Xiao, H. Zhang, X. F. Yu, *Adv. Opt. Mater.* **2016**, 4, 1223.

[39] A. H. Woomer, T. W. Farnsworth, J. Hu, R. A. Wells, C. L. Donley, S. C. Warren, *ACS Nano* **2015**, 9, 8869.
[40] F. Luo, D. Wang, J. Zhang, X. Li, D. Liu, H. Li, M. Lu, X. Xie, L. Huang, W. Huang, *ACS Appl. Nano Mater.* **2019**, 2, 3793.
[41] J. M. Urban, M. Baranowski, A. Surrente, D. Wlodarczyk, A. Suchocki, G. Long, Y. Wang, L. Klopotowski, N. Wang, D. K. Maude, P. Plochocka, *Nanoscale* **2017**, 9, 19298.
[42] H. B. Ribeiro, M. A. Pimenta, C. J. S. de Matos, *J. Raman Spectrosc.* **2018**, 49, 76.
[43] Z. Guo, H. Zhang, S. Lu, Z. Wang, S. Tang, J. Shao, Z. Sun, H. Xie, H. Wang, X.-F. Yu, P. K. Chu, *Adv. Funct. Mater.* **2015**, 25, 6996.
[44] B. Tian, B. Tian, B. Smith, M. C. Scott, R. Hua, Q. Lei, Y. Tian, *Nat. Commun.* **2018**, 9, 1397.
[45] F. L. Galeener, J. J.C. Mikkelsen, *Solid State Commun.* **1979**, 30, 505.
[46] T. Zhang, Y. Wan, H. Xie, Y. Mu, P. Du, D. Wang, X. Wu, H. Ji, L. Wan, *J. Am. Chem. Soc.* **2018**, 140, 7561.
[47] H. Xiang, Y. Nie, H. Zheng, X. Sun, X. Sun, Y. Song, *Chem. Commun.* **2019**, 55, 8094.
[48] T. Ramireddy, T. Xing, M. M. Rahman, Y. Chen, Q. Dutercq, D. Gunzelmann, A. M. Glushenkov, *J. Mater. Chem. A* **2015**, 3, 5572.
[49] S. Z. Mortazavi, P. Parvin, A. Reyhani, *Laser Phys. Lett.* **2012**, 9, 547.
[50] D. Reyes-Contreras, M. Camacho-López, M. A. Camacho-López, S. Camacho-López, R. I. Rodríguez-Beltrán, M. Mayorga-Rojas, *Opt. Laser Technol.* **2015**, 74, 48.
[51] M. Qian, Y. P. Niu, S. Q. Gong, *Appl. Surf. Sci.* **2018**, 428, 549.
[52] D. Zhang, J. Liu, P. Li, Z. Tian, C. Liang, *ChemNanoMat* **2017**, 3, 512.
[53] Z. L. Xu, S. Lin, N. Onofrio, L. Zhou, F. Shi, W. Lu, K. Kang, Q. Zhang, S. P. Lau, *Nat. Commun.* **2018**, 9, 4164.
[54] G. A. Bhat, S. Haldar, S. Verma, D. Chakraborty, R. Vaidhyanathan, R. Murugavel, *Angew. Chem. Int. Ed.* **2019**, 58, 16844.
[55] J. Texter, *Angew. Chem. Int. Ed.* **2015**, 54, 10258.
[56] Z. Y. Xia, S. Pezzini, E. Treossi, G. Giambastiani, F. Corticelli, V. Morandi, A. Zanelli, V. Bellani, V. Palermo, *Adv. Funct. Mater.* **2013**, 23, 4684.
[57] H. Sadeghi, E. Solati, D. Dorranian, *J. Laser Appl.* **2019**, 31, 042003.
[58] *CRC Handbook of Chemistry and Physics*, CRC Press, 2019.
[59] H. Jin, H. Wang, Z. Qi, D. S. Bin, T. Zhang, Y. Wan, J. Chen, C. Chuang, Y. R. Lu, T. S. Chan, H. Ju, A. M. Cao, W. Yan, X. Wu, H. Ji, L. J. Wan, *Angew. Chem. Int. Ed.* **2020**, 59, 2318.
[60] S. Haldar, K. Roy, R. Kushwaha, S. Ogale, R. Vaidhyanathan, *Adv. Energy Mater.* **2019**, 9, 1902428.
[61] S. Haldar, K. Roy, S. Nandi, D. Chakraborty, D. Puthusseri, Y. Gawli, S. Ogale, R. Vaidhyanathan, *Adv. Energy Mater.* **2018**, 8, 1702170.
[62] Q.-F. Li, C.-G. Duan, X. G. Wan, J.-L. Kuo, *J. Phys. Chem. C* **2015**, 119, 8662.
[63] K. Roy, M. Wahid, D. Puthusseri, A. Patrike, S. Muduli, R. Vaidhyanathan, S. Ogale, *Sustain. Energy Fuels* **2019**, 3, 245.
[64] A. E. Del Rio Castillo, V. Pellegrini, H. Sun, J. Buha, D. A. Dinh, E. Lago, A. Ansaldo, A. Capasso, L. Manna, F. Bonaccorso, *Chem. Mater.* **2018**, 30, 506.
[65] M. Dahbi, N. Yabuuchi, M. Fukunishi, K. Kubota, K. Chihara, K. Tokiwa, X.-f. Yu, H. Ushiyama, K. Yamashita, J.-Y. Son, Y.-T. Cui, H. Oji, S. Komaba, *Chem. Mater.* **2016**, 28, 1625.
[66] Y. Zhang, X. Rui, Y. Tang, Y. Liu, J. Wei, S. Chen, W. R. Leow, W. Li, Y. Liu, J. Deng, B. Ma, Q. Yan, X. Chen, *Adv. Energy Mater.* **2016**, 6, 1502409.

[67] Y. Zhang, H. Wang, Z. Luo, H. T. Tan, B. Li, S. Sun, Z. Li, Y. Zong, Z. J. Xu, Y. Yang, K. A. Khor, Q. Yan, *Adv. Energy Mater.* **2016**, 6, 1600453.
[68] G. Ning, B. Haran, B. N. Popov, *J. Power Sources* **2003**, 117, 160.
[69] S. Wang, Q. Wang, P. Shao, Y. Han, X. Gao, L. Ma, S. Yuan, X. Ma, J. Zhou, X. Feng, B. Wang, *J. Am. Chem. Soc.* **2017**, 139, 4258.
[70] Z. Yu, J. Song, M. L. Gordin, R. Yi, D. Tang, D. Wang, *Adv. Sci.* **2015**, 2, 1400020.
[71] W. Xue, L. Miao, L. Qie, C. Wang, S. Li, J. Wang, J. Li, *Curr. Opin. Electrochem.* **2017**, 6, 92.

List of figures

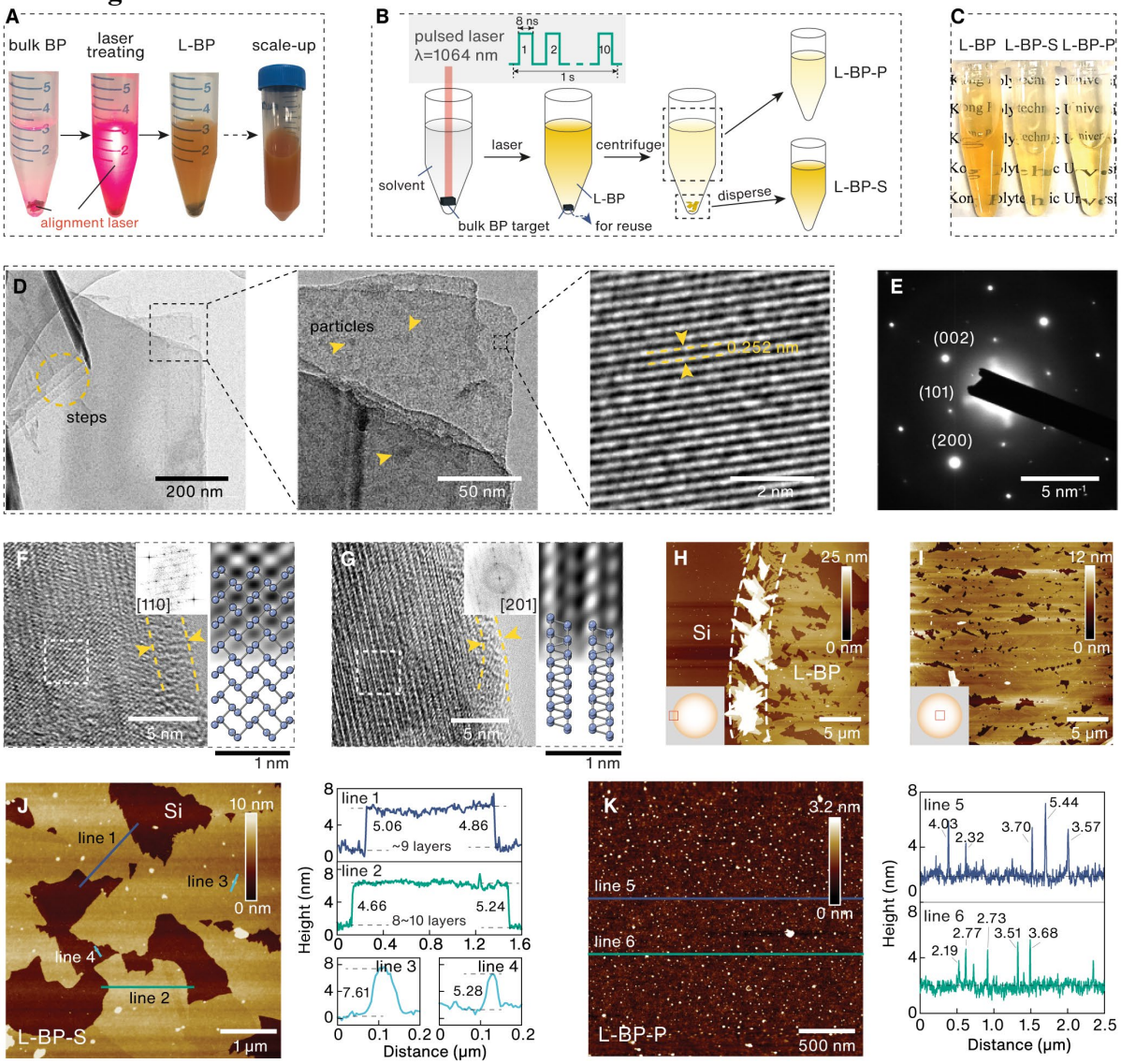

Figure 1 Preparation and morphological characterization of laser-treated BP products. (**A**) Digital images of the solution corresponding to preparation procedures and the scale-up product (laser treatment in 2-propanol). (**B**) Schematic illustration of the preparation procedure. The laser sequence is shown as the inset. (**C**) Digital images of as-prepared L-BP, L-BP-S, and L-BP-P suspension in 2-propanol. **(D)** TEM images of L-BP featuring steps (indicated by the yellow circle), particles (indicated by the yellow arrow), and nanosheets. **(E)** SAED pattern of the black dotted rectangle region shown in **D**. (**F, G**) TEM images of L-BP-S nanosheets viewed in the crystallographic projection along the (**F**) (110) and (**G**) (201) zone axis (ZA).

Yellow arrow and lines indicate the amorphous region. Insets are the FFT of the areas highlighted with white dashes as well as the real and corresponding simulated structure models. (**H, I**) AFM images of the ring stain formed by L-BP drop-cast on a SiO_2/Si wafer substrate at selected regions: (**H**) edge and (**I**) center. (**J, K**) AFM images and line profiles of (**J**) L-BP-S and (**K**) L-BP-P, featuring mainly nanosheets and nanoparticles, respectively.

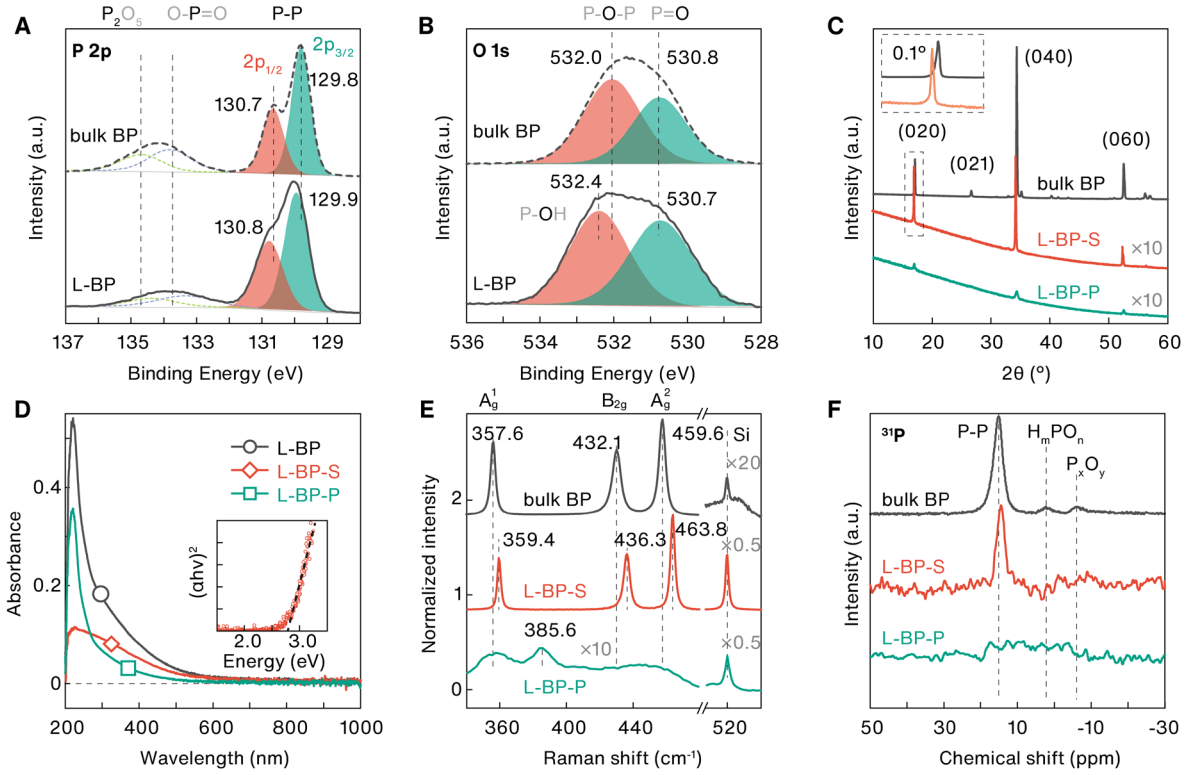

Figure 2 Spectroscopic characterization of laser-treated BP products. (**A, B**) XPS spectra of bulk BP and L-BP in (**A**) P 2*p* and (**B**) O 1*s* regions. **(C)** XRD patterns of bulk BP, L-BP-S, and L-BP-P. (**D**) UV-vis spectra of L-BP, L-BP-P, and L-BP-S suspended in 2-propanol. Inset shows the direct Tauc plots of L-BP-S for the high-energy band-to-band transition determination. (**E**) Raman spectra of bulk BP, L-BP-P, and L-BP-S using a 532 nm excitation laser at an energy power of 650 mJ. (**F**) ^{31}P MAS ssNMR spectra of bulk BP, L-BP-P, and L-BP-S at the spinning speed of 10 kHz.

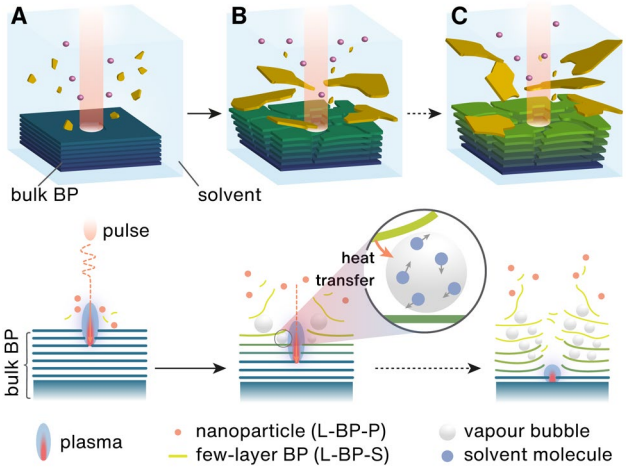

Figure 3 Proposed mechanism of pulsed laser-assisted few-layer BP preparation. (**A**) Initial phase producing mainly L-BP-P. (**B**) Exfoliation phase producing both L-BP-S and L-BP-P. (**C**) Mass production of L-BP-S.

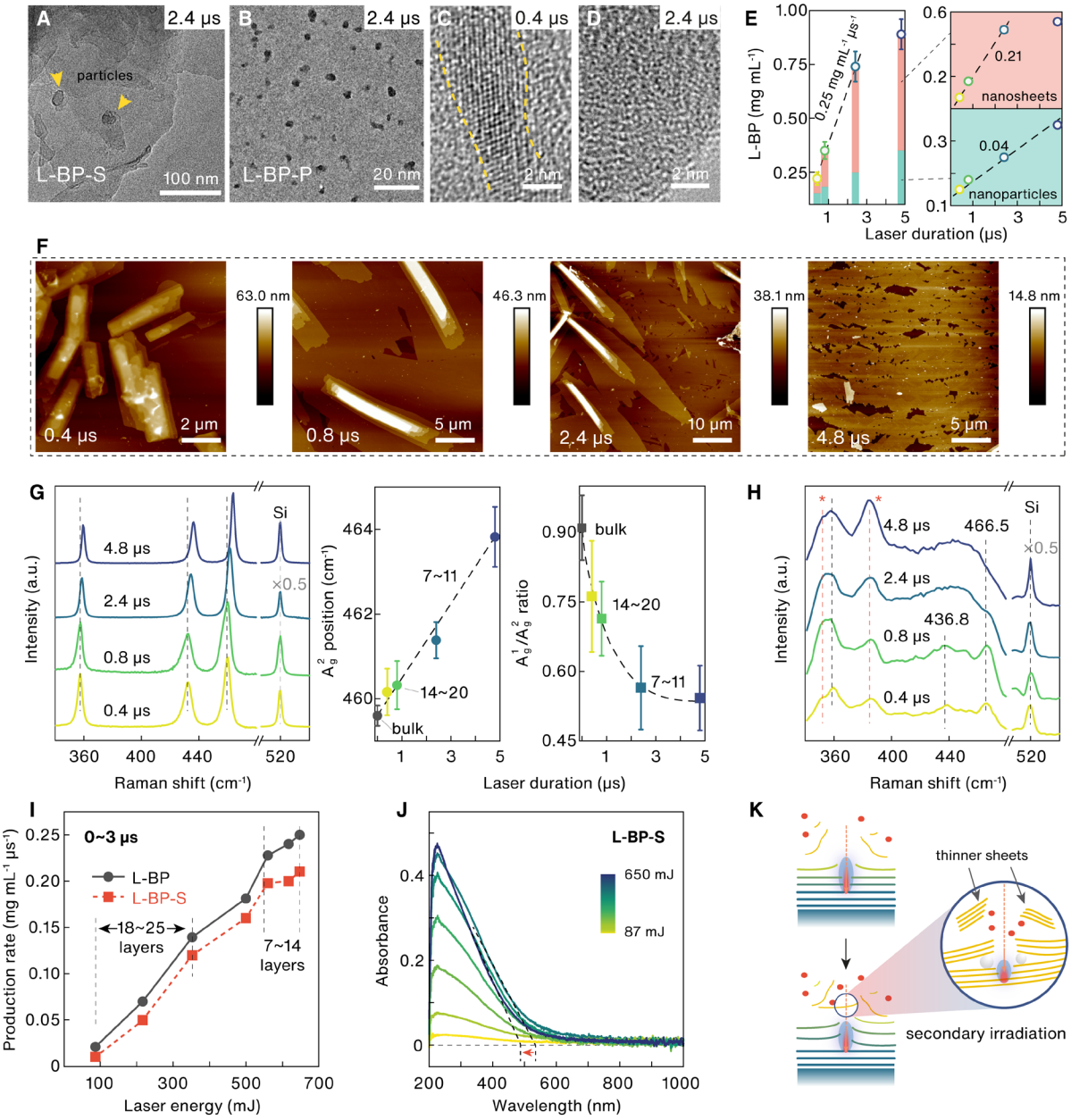

Figure 4 Effect of laser duration and energy on the structure of L-BP products. (**A, B**) TEM images of L-BP-S and L-BP-P with a laser duration of 2.4 μs. (**C, D**) TEM images of L-BP-P produced with a laser duration of (**C**) 0.4 μs and (**D**) 2.4 μs. (**E**) Correlation between laser duration and L-BP (L-BP-S and L-BP-P) concentration in 2-propanol. The proportion of L-BP-S (nanosheets) and L-BP-P (nanoparticles) are shown in orange and grey, respectively. (**F**) AFM images of L-BP-S prepared with variou laser irradiation durations. (**G**) Raman spectra of L-BP-S with different laser duration from 0.4 to 4.8 μs and the correlation between laser

duration, A_g^2 peak position and A_g^1/A_g^2 intensity ratio of L-BP-S. (**H**) Raman spectra of L-BP-P with different laser duration from 0.4 to 4.8 μs. (**I**) Correlation between the laser energy and the production rate of L-BP and L-BP-S (from 0 to 3 μs). (**J**) UV-vis spectra of L-BP-S suspended in 2-propanol produced using different laser energy with a fixed laser duration of 3 μs. (**K**) Illustration of thinner BP nanosheets production via secondary irradiation.

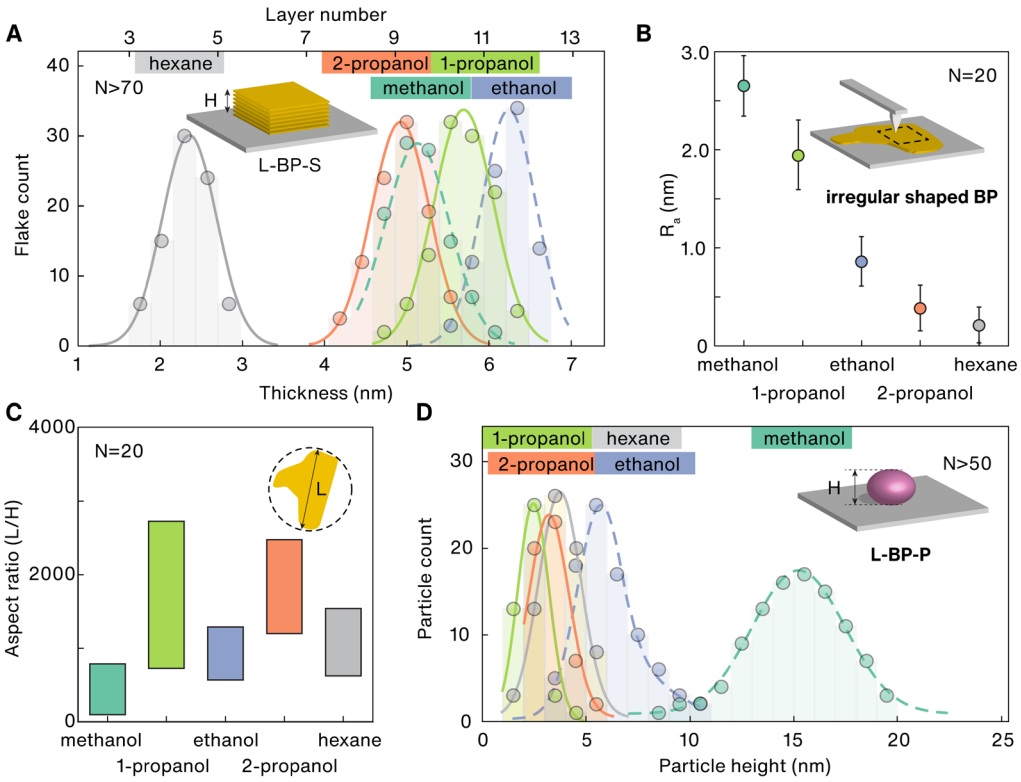

Figure 5 Effect of solvent on the morphology of L-BP products. (**A**) Height distribution of L-BP-S produced in various solvents (laser duration = 4.8 μs): methanol, ethanol, 1-propanol, 2-propanol, and hexane. (**B**) The surface height (R_a, arithmetic average of the absolute values) of as-prepared L-BP-S nanosheets. The step regions between SiO_2 and BP nanosheets are avoided (illustrated as inset). (**C**) Aspect ratio (L/H) of as-prepared L-BP-S nanosheets. Inset shows the definition of L. 20 flakes were measured for R_a and L/H. (**D**) Height distribution of L-BP-P produced in various solvents (laser duration = 4.8 μs).

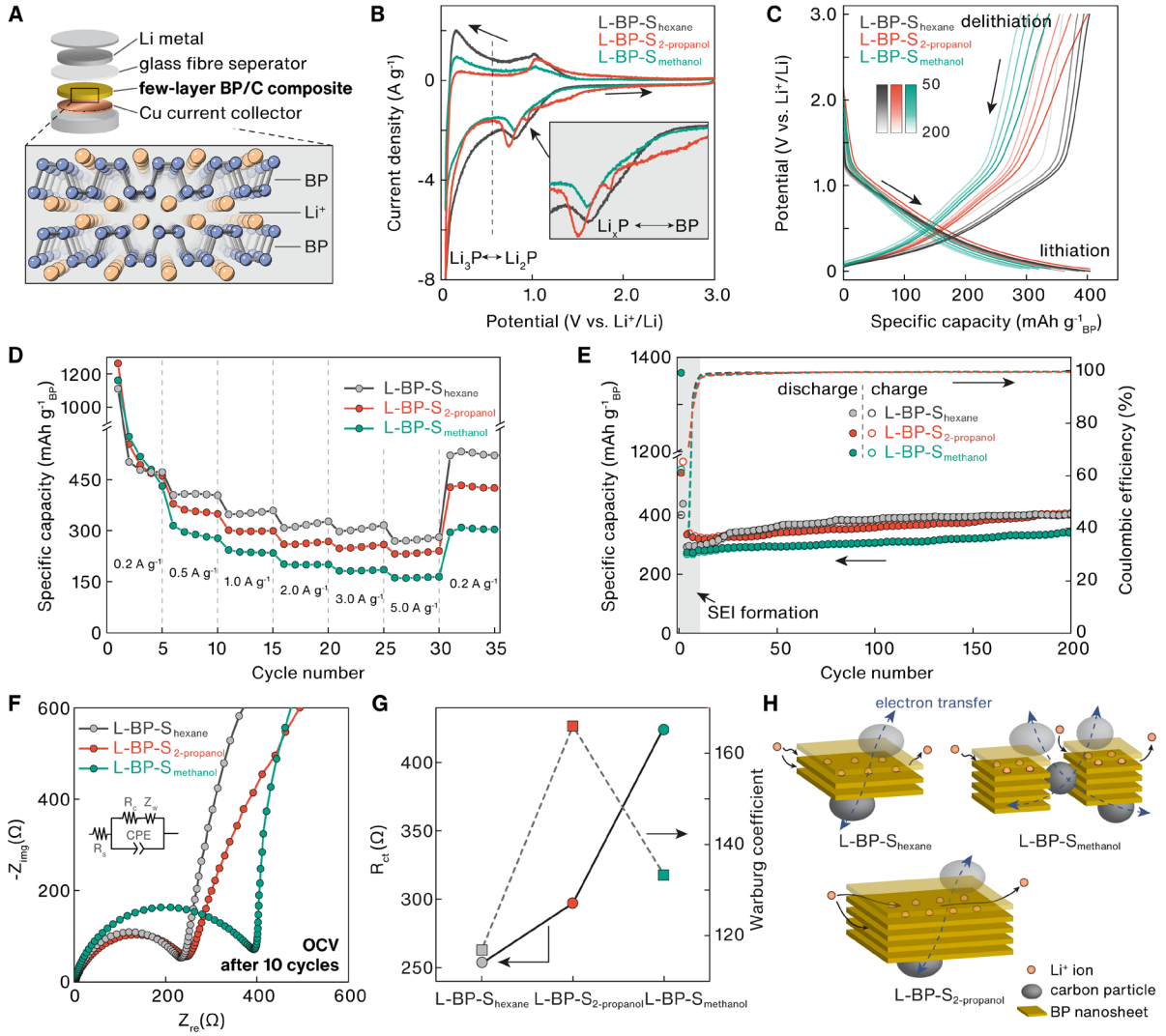

Figure 6 Performance of LIBs using L-BP-S exfoliated in different solvents (hexane, 2-propanol, and methanol) as the anode material. (**A**) Illustration of the LIB structure and the structural representation of Li^+ ion transport channels in a few-layer BP. (**B**) Cyclic voltammograms (first cycle) of LIBs within 0.05~3.0 V at a scan rate of 0.03 mV s^{-1}. Discharge current peaks are labelled from BP to Li_3P formation. (**C**) Voltage profiles of the 50th, 100th, 150th, and 200th cycle upon the galvanostatic charge/discharge of LIBs at 1.0 A g^{-1} between 0.001 and 3.0 V. (**D**) Specific capacity of LIBs over galvanostatic charge/discharge cycles between 0.001 and 3.0 V at various specific currents (0.2, 0.5, 1.0, 2.0, 3.0, and 5.0 A g^{-1}). (**E**) Specific capacity and Coulombic efficiency of LIBs over 200 galvanostatic charge/discharge cycles between 0.001 and 3.0 V at 1.0 A g^{-1}. (**F**) GEIS Nyquist plots of fully charged LIBs (at

OCV after 10 cycles) with an amplitude current of 0.5 mA RMS. The inset is the equivalent circuit model. (**G**) Fitted charge transfer resistance and Warburg coefficient values based on GEIS plots. (**H**) Proposed mechanism of Li^+ diffusion in L-BP-S nanosheets of different morphology.

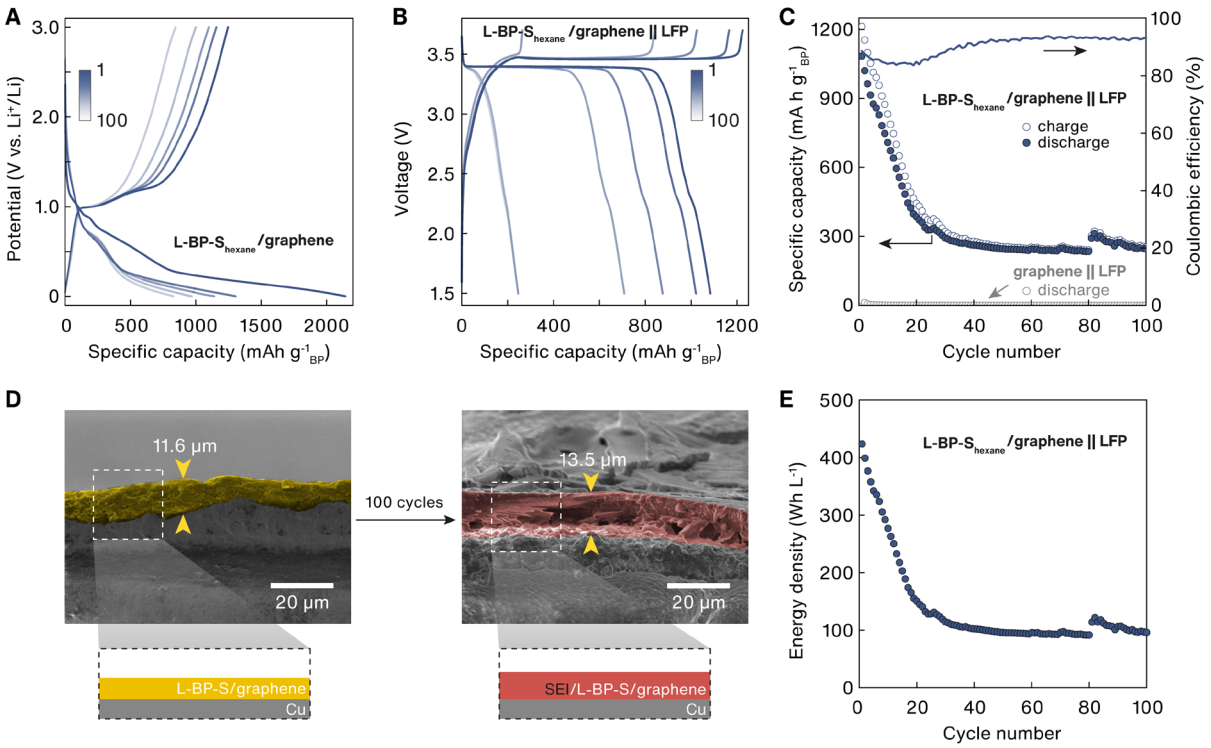

Figure 7 Half-cell and full-cell performance of graphene-modified L-BP-S anode. (**A, B**) Voltage profiles upon the galvanostatic charge/discharge of (**A**) L-BP-S_{hexane}/graphene anode half-cell at 0.2 A g^{-1} between 0.001 and 3.0 V (1st, 25th, 50th, 75th, and 100th cycles), and (**B**) L-BP-S_{hexane}/graphene||LFP full-cell at 0.1 A g^{-1} between 1.5 and 3.7 V (1st, 2nd, 5th, 10th, 50th, and 100th cycles). (**C**) Specific capacity and Coulombic efficiency of full-cell over 100 galvanostatic charge/discharge cycles between 1.5 and 3.7 V. (graphene||LFP full-cell data is shown for comparison). (**D**) Cross-sectional SEM images of L-BP-S_{hexane}/graphene anode before and after 100 cycles in full-cell. The active material layer is highlighted in yellow. (**E**) Volumetric energy density of the L-BP-S_{hexane}/graphene||LFP full-cell over 100 cycles.

table of contents

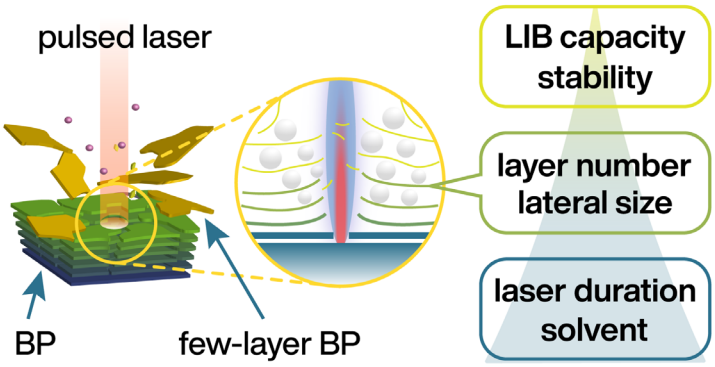

Tuning BP thickness with laser. A liquid-phase exfoliation method assisted by pulsed laser is described. The layer number and lateral size of few-layer BP depend on the laser duration and solvent. Such few-layer BP enables the study of the relationship between morphology and BP-based anode performance, showing thinner thickness and smaller lateral size promote faster Li^+ ion transport.

Keyword *black phosphorus; laser-assisted exfoliation; morphology control; Li-ion battery; morphological effect*

Weiran Zheng[†] *Jeongyeon Lee,*[†] *Zhi-Wen Gao, Yong Li, Shenghuang Lin, Shu Ping Lau,* Lawrence Yoon Suk Lee**

Laser-assisted Ultrafast Exfoliation of Black Phosphorus in Liquid with Tunable Thickness for Li-ion Batteries